Journal of Membrane Science 636 (2021) 119559

Contents lists available at ScienceDirect

Journal of Membrane Science

journal homepage: www.elsevier.com/locate/memsci

Water channel structure of alternative perfluorosulfonic acid membranes for fuel cells

Santiago P. Fernandez Bordín [a,b], Heber E. Andrada [a,b], Alejo C. Carreras [a,b], Gustavo Castellano [a,b,*], Ralf Schweins [c], Gabriel J. Cuello [c], Claudia Mondelli [d], Víctor M. Galván Josa [a,b]

[a] *Universidad Nacional de Córdoba, Facultad de Matemática, Astronomía, Física y Computación, Argentina*
[b] *Instituto de Física Enrique Gaviola (IFEG), CONICET – Medina Allende s/n, Ciudad Universitaria (5000) Córdoba, Argentina*
[c] *Institut Laue–Langevin, DS, 71 Avenue des Martyrs, CS 20 156, 38042 Grenoble Cedex 9, France*
[d] *CNR-IOM, Institut Laue–Langevin, 71 Avenue des Martyrs 38042 Grenoble Cedex 9, France*

ARTICLE INFO

Keywords:
Fuel cells
Polymer electrolyte membrane
Direct methanol fuel cell
SANS
Monte Carlo simulation

ABSTRACT

The use of fuel cells is strategic in the global energy system; their inclusion in eco-cars, avoiding CO_2 emission, represents a crucial enhancement for the environment. For this reason, any improvement in their use and optimization is fundamental for our society. Since one of the main components in these cells is their polymeric proton exchange membrane, in this work, the commercial Fumapem F-14100 and F-1850 membranes have been studied, both representing a cheap and effective alternative in direct methanol fuel cell (DMFC) applications. Their characterization will provide a new insight about them, in order to optimize and improve future fuel cell operation conditions. Small angle neutron scattering (SANS) has been used in this work to achieve a nanometric structural characterization of these membranes, which is key for understanding their physicochemical properties. Starting from SANS measurements, empirical fitting models were applied in order to obtain global sample features, which allowed to propose a lamellar water channel structure. Then, 2D scattering length density maps generated by Monte Carlo simulations were optimized to match the experimental SANS intensity profiles by using the inverse Fourier transform method. In addition, the crystalline contribution from the sample ordered domains was also studied by using X-ray diffraction.

1. Introduction

In the last two decades, the global consumption of primary energy has increased exponentially, positioning the use and production of energy resources as one of the biggest current issues. Even though renewable energy development has increased significantly in recent decades, the current energy consumption depending on fossil fuels reaches approximately 80% [1] resulting in greenhouse gas emissions, climate changes, and other environmental issues. In this context, proton exchange membrane fuel cells (PEMFCs) have been established as a promising alternative energy source, which have the potential to replace fossil fuel technology and energy sources even for mobile devices [2,3]. In the area of fuel cells, direct methanol fuel cells (DMFCs) have also deserved attention due to the good properties of methanol, such as its high energy density, and the fact that it can be easily transported and stored [4,5].

A key component in PEMFCs are the proton exchange membranes. They consist of synthetic polymeric membranes with functional groups ionizable and permeable to protons, and are intended to allow proton exchange in aqueous solution [6]. Their function is to transport ionic charges from the anode to the cathode, closing the circuit of the electrochemical cells. In addition, they must act as a barrier preventing fuel crossover, which reduces the efficiency of these cells. As widely reported in the literature, for PEMFC applications, these membranes are expected to bear high proton conductivity; high mechanical, thermal and chemical stability; high proton exchange capacity; low electronic conductivity and low fuel and oxidant permeability [7–12].

One of the most common and commercially available proton exchange membranes used as electrolytes is the Nafion® membrane, produced by DuPont; it consists of a tetrafluoroethylene copolymer and a vinyl ether with a sulfonyl fluoride group at the end, its channel structure being widely discussed [13,14]. Currently, research efforts are being made to develop alternative membranes, cheaper than Nafion® and with a similar or higher conductivity and lower fuel crossover in the

---

[*] Corresponding author at: Universidad Nacional de Córdoba, Facultad de Matemática, Astronomía, Física y Computación, Argentina.
E-mail address: gcas@famaf.unc.edu.ar (G. Castellano).

https://doi.org/10.1016/j.memsci.2021.119559
Received 15 December 2020; Received in revised form 23 June 2021; Accepted 25 June 2021

temperature range of interest (25–100°C) [15–17]. Several types of proton exchange membranes are being investigated at present, including sulfonated polyethersulfones [18], sulfonated polysulfones [19], sulfonated polyether ketones [20], sulfonated polyimide [21], sulfonated or acid doped polybenzimidazole [22–24] with the aim of reducing fuel crossover in direct methanol cells [25].

Recently, FuMATech laboratories have developed low-cost fumion® membranes based on a perfluorinated sulfonic acid (PFSA) ionomer of long side chain and molecular weight a bit higher than that of the standard N-117 Nafion® (1100 g/mol). On the other hand, the Fumapem® F-1850 and F-14100 membranes are respectively 50 μm and 100 μm thick, whereas the N-117 Nafion thickness is 175 μm. The use of high equivalent weight PFSA membranes for DMFC applications, instead of the standard ionomer PFSA ones, reduces the detrimental effect of methanol crossover and the excessive swelling of the membrane, due to the lower amount of sulfonic groups per unit volume, since the channels are less hydrophilic [25]. These Fumapem membranes bear thicknesses smaller than the standard N-117 Nafion®, achieving similar (or even higher) conductivities [26,27].

The potential impact of the effect of morphology of PEMs on electrochemical performance and stabilities may be extremely important [11]; nevertheless, at present no systematic characterization using small angle scattering techniques has been reported for these membranes, in spite of their good performances and their inexpensive cost —around 50% the prices of Nafion® membranes, according to commercial web sites. Although wide-angle X-ray scattering (WAXS) studies have been performed on these membranes [28], only the crystalline and amorphous structural information has been reported. Small angle scattering techniques provide information regarding the water channel density and shape, intimately related to ionic conductivity. In this work, the structural properties of Fumapem F-1850 and F-14100 membranes [10,26] were studied by means of small-angle neutron scattering (SANS), a technique which has proven to be successful in similar studies [29–31]. Considering the global features associated with empirical models (i.e. sample main correlation length, channel shape and size, etc.), a structural model is proposed here, based on lamellar water channels surrounded by a hydrophilic layer formed by sulfonic chains. Scattering length density maps corresponding to inverse core–shell water channel lamellar clusters were generated by Monte Carlo simulations. The resulting Fumapem structures were obtained by optimizing the parameters involved in the simulations, to achieve the best match with the experimental SANS profiles.

The results achieved here in the nanometer region allow to relate membrane structural features to their efficiency, specifically protonic conductivity and low permeability to both methanol and ethanol. This low permeability is one of the main reasons to encourage the use of these membranes in direct alcohol fuel cells.

2. Materials and methods

Commercial Fumapem 100 μm-thick F-14100 and 50 μm-thick F-1850 membranes (~3 cm^2) were subjected to an activation treatment (see, e.g., ref. [32]), intended to protonate the sulfonic groups, which are the membrane active sites. This procedure consists of:

- heating in Milli-Q water up to 80°C, and keep this temperature for 1 h;
- rinsing with Milli-Q water;
- heating in hydrogen peroxide (H_2O_2) 3% solution up to 80°C, and keep this temperature for 1 h;
- rinsing with Milli-Q water;
- heating in a 0.5 M sulfuric acid (H_2SO_4) solution up to 80°C, and keep this temperature for 1 h;
- rinsing with Milli-Q water;
- keep under water.

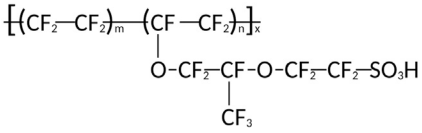

Fig. 1. General chemical structure for the copolymer Fumapem membranes.

With the aim of assessing the structural changes produced by this activation procedure, samples with and without treatment were studied (suffixes T and U, respectively).

These proton exchange membranes are based on fluorocarbon and perfluorosulfonic acid-type polymers, in which different equivalent weights and thickness have been tried. Fig. 1 displays a schematic diagram for the chemical structure corresponding to these membranes, as illustrated in [28]. It is worth mentioning that limited information is available regarding this structure detail. According to the manufacturers, the ion-exchange capacities (0.45–0.7 meq/g) and consequent conductivities (40–72 mS/cm) for Fumapem F-14100 and F-1850 are somewhat lower than those corresponding to similar Nafion® membranes (0.9–1 meq/g and 100 mS/cm); this suggests a less frequent occurrence of the sulfonic groups responsible for proton exchange, which may be associated to higher m values in the arrangement depicted in Fig. 1, where some authors have readily set $n = x = 1$ (see e.g. [33]). Both membranes are delivered on PET backing foils, and their dimensional swelling ratio is 4%–6% for F-14100 and 8%–10% for F-1850, always as reported in the manufacturers' technical datasheets.

The structural model proposed here has been inferred from the general features surveyed for the membranes, after fitting empirical models to the experimental patterns acquired. This information therefore allows to furnish two-dimensional scattering-length density maps, which are finally fitted through Monte Carlo simulations, as detailed below. The empirical models available constitute an important tool when dealing for the first time with SANS patterns, allowing to reveal the main trends. To this aim, the Guinier–Porod model (GPM) suggested by Hammouda [34] was applied at the low-q region; this model allows to obtain information about the shape and size of the scattering object and is valid for elongated objects such as rods or lamellae [35,36]

$$I(q) = \begin{cases} \dfrac{G}{q^s} \exp\left(\dfrac{-q^2 R_g^2}{3-s}\right) & \text{for} \quad q \le q_1 \\[2ex] \dfrac{D}{q^d} & \text{for} \quad q \ge q_1 \, , \end{cases} \tag{1}$$

where G and D are scaling factors, d is the Porod exponent, R_g is the gyration radius, the s parameter accounts for nonspherical objects, and q_1 is defined to provide appropriate continuity conditions to match both expressions. For spheres, $s = 0$; for rods $s = 1$, and for lamellae $s = 2$.

Complementary, the addition of two models was chosen for the high-q region: the broad peak model (BPM) and the correlation length model (CLM). The first one (BPM) is associated to characteristic distances (d-spacing) between scattering inhomogeneities; the second one (CLM) applies to scattering objects of different sizes [37], and accounts for the continuum signal associated to the amorphous polymer matrix and the crystalline domains

$$I(q) = \frac{C_1}{1 + (|q - q_o|\xi_1)^{m_1}} + \frac{1}{q^\ell} \frac{C_2}{1 + (q\xi_2)^{m_2}} + B \, , \tag{2}$$

where C_i are scaling factors, the peak centroid position $q_o = 2\pi/d_o$ may be related to the average spacing d_o between the lamellae present in the sample [38], ξ_i represent the correlation lengths, m_i are the high-q Porod exponents, the parameter ℓ is a stretching factor, and B represents the background [39].

All the parameters related with these empirical models were obtained through fittings using the FindFit function in the Mathematica® software package.

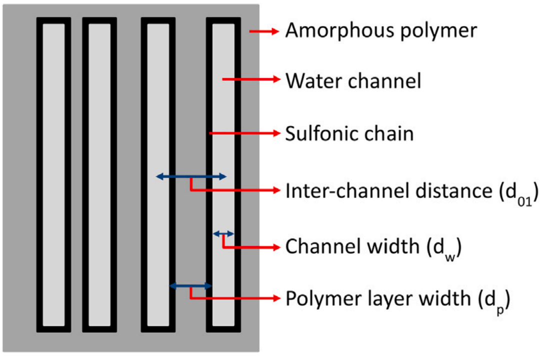

Fig. 2. Scheme of a finished cluster. Light gray: water channel, black: sulfonic chain, dark gray: amorphous polymer.

As described in the following section, the fittings carried out with the above-mentioned empirical models impose certain characteristic parameters (main correlation length, channel shape and size, etc.) that must be involved in the Monte Carlo simulation geometry. After several attempts based on the different structural models proposed in the literature, the lamellar water channel structure, which has already been suggested for similar membranes [14,40,41], was revealed by these empirical model fittings; all these features must be accounted for in order to furnish appropriate scattering length density maps, as considered in the simulations. The membrane structures were thus generated by randomly placing these clusters in an amorphous polymer matrix (apm), taking care to avoid overlapping. The procedure for this construction is similar to that followed in ref. [42], and Fig. 2 shows an example cluster scheme. The parameters involved in the generation of each cluster are: the cluster radius, the number of channels per cluster, the mean inter-channel distance, the channel width and a disorder parameter for the inter-channel distance distribution. Briefly, the cluster generation procedure begins by fitting the cluster radius for the membrane 2D cross sections, which delimits each lateral channel domain; once this radius is set, its value remains fixed in the final simulation step. The number of channels for this domain is stochastically chosen at each stage, ranging between minimum and maximum values previously established. Also the azimuth lamellar orientation is randomly generated, after which these channels are sequentially allocated within the polymer matrix; the inter-channel distance $d_{01} = d_p + d_w$ is almost constant, since although the channel width d_w is fixed, the polymer layer between water channels is allowed to vary around a mean value d_p, following a uniform probability distribution with a Δ_p width. A shell 0.7–1 nm thick (uniform random distribution) was then added to each channel, corresponding to the sulfonic chains. Once each cluster is ready, it is also randomly allocated inside the amorphous polymer matrix: if the sampled position attempts to overlap with an already allocated cluster, a new position is generated until channels will not enter in contact. In this way, clusters are successively placed until the density map is completed, or alternatively a loop counter reaches an upper limit before the sampling algorithm is able to find an available location. SANS profiles were then assessed following Schmidt–Rohr [43], i.e. modeling the scattering intensity as a function of q, by using the Inverse Fourier Transform in a two-dimensional scattering length density map for long parallel structures. The scattering length densities (SLD) used were taken from ref. [29]: $\mathrm{SLD}_{\mathrm{apm}} = 4.07 \times 10^{-6}$ Å^{-2} with $\rho = 2.0$ g/cm^3 and $\mathrm{SLD}_{\mathrm{H_2O}} = -5.6 \times 10^{-7}$ Å^{-2} with $\rho = 1.0$ g/cm^3. For the sulfonic chains (sc), initial estimates for ρ and SLD were inferred from the data provided by Schmidt–Rohr and Chen [13]; additional estimates for these parameters were obtained by assessing them from raw covalent bond radii, and taking into account possible SLDs variations, as reported in [44] for similar materials. The final values for these parameters were fitted along the simulation process, obtaining $\mathrm{SLD}^{\mathrm{T}}_{\mathrm{sc}} = 9.43 \times 10^{-6}$ Å^{-2} for the treated membrane, and $\mathrm{SLD}^{\mathrm{U}}_{\mathrm{sc}} = 6.9 \times 10^{-6}$ Å^{-2} for the untreated one.

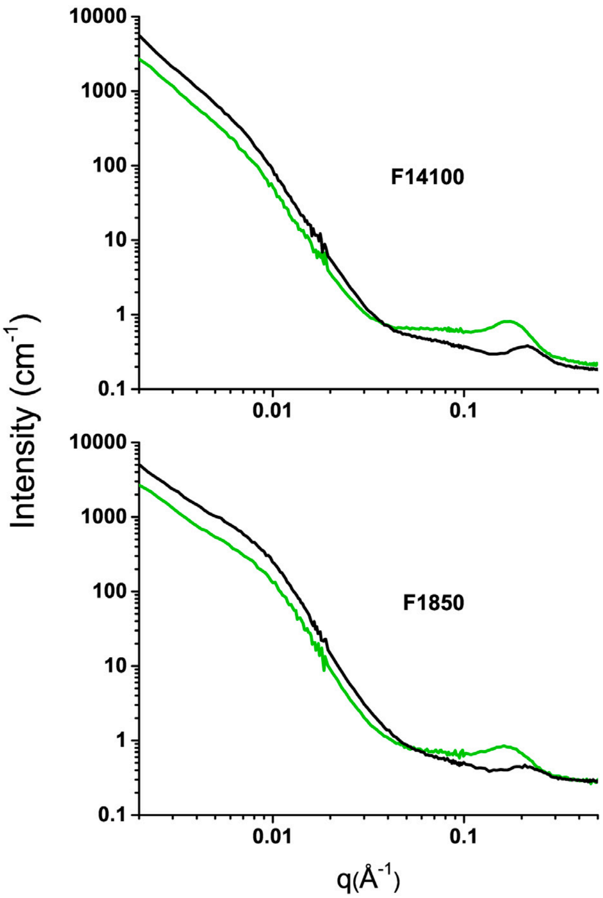

Fig. 3. Full range experimental SANS patterns. Green: treated; black: untreated. (For interpretation of the references to color in this figure legend, the reader is referred to the web version of this article.)

Table 1
Low-q fitting parameters for Eq. (1).

Sample	s	d	R_g(Å)
F14100U	1.97 ± 0.08	3.85 ± 0.04	91 ± 5
F14100T	1.98 ± 0.04	3.74 ± 0.05	90 ± 5
F1850U	1.36 ± 0.05	4.06 ± 0.05	90 ± 2
F1850T	1.45 ± 0.06	3.99 ± 0.08	82 ± 3

Another structural contribution comes from the small polymer crystalline domains distributed all along the amorphous matrix. In order to provide an adequate estimate of this crystalline contribution in our model, the SASfit software [45] was used. To this aim, the curve obtained from the correlation length model was used as input, obtaining a form factor estimate for the crystals, as detailed below.

The Fumapem structure approach was obtained by adding the different curves corresponding to simulations, SASfit software and the background; an optimization of all the parameters involved allowed to achieve the best fit to the experimental profile. It is worth mentioning that the whole process involved different geometrical configurations, among which the best suited is that shown in next section, which will be discussed in detail.

3. Experimental

SANS measurements were performed on the D11 instrument at the Institut Laue–Langevin, Grenoble, France [46]. The incoming wavelength was $\lambda = 5$ Å and three sample-to-detector distances were set:

Table 2
High-q fitting parameters.

Sample	C_1	q_{01} (Å^{-1})	ξ_1 (Å)	m_1	C_2	ℓ	ξ_2 (Å)	m_2	B
F14100U	0.16 ± 0.01	0.217 ± 0.001	25 ± 1	2.3 ± 0.1	0.33 ± 0.05	0.13 ± 0.01	13 ± 1	2.0 ± 0.1	0.18 ± 0.01
F14100T	0.49 ± 0.05	0.177 ± 0.001	22 ± 1	2.4 ± 0.1	0.44 ± 0.05	0.00 ± 0.01	9 ± 1	3.2 ± 0.1	0.21 ± 0.01
F1850U	0.13 ± 0.02	0.213 ± 0.002	24 ± 1	2.5 ± 0.1	0.42 ± 0.05	0.22 ± 0.05	17 ± 1	2.1 ± 0.1	0.28 ± 0.01
F1850T	0.47 ± 0.09	0.168 ± 0.002	20 ± 1	2.4 ± 0.1	0.25 ± 0.05	0.27 ± 0.02	10 ± 1	2.7 ± 0.3	0.24 ± 0.01

1.4, 8 and 39 m. These configurations allowed to explore the scattering vector q on the range between 0.002 and 0.55 Å^{-1}. All samples were measured at ambient moisture and temperature.

In order to study the crystallinity of the samples, X-ray diffraction (XRD) patterns were acquired in a PANalytical X'Pert Pro diffractometer with a copper tube and a graphite monochromator attached. The conditions set for the present measurements were 40 kV and 40 mA, 0.02° step size and the effective counting time was 100 s/step.

4. Results and discussion

Fig. 3 displays experimental SANS patterns for the Fumapem treated and untreated membranes. All four curves exhibit similar features: three linear regions with slope changes at $q \sim 0.01$ Å^{-1} and $q \sim 0.04$ Å^{-1}, and a broad and well defined peak above 0.1 Å^{-1}. The main difference between treated and untreated samples is evidenced in the position and intensity of these peaks.

As mentioned above, to analyze the patterns using the empirical models, they were split into two regions, below and above $q \sim 0.045$ Å^{-1} where the second slope change occurs. From the low-q region, features related to size and shape of the scattering objects can be inferred, whereas from the high-q region structural information can be withdrawn, and the correlation between objects can be analyzed. Fig. 4 shows the low-q fitting profile using the GPM approach, the resulting parameters being displayed in Table 1. As mentioned above, the s parameter is related to the shape of the scattering object. For F14100 membranes $s \approx 2$, which means the scattering objects are mainly lamellae [38]. On the other hand, for F1850 samples $s \approx 1.4$, which may be associated to a mixture of rods ($s = 1$) and lamellae ($s = 2$). The parameter d gives information about the scattering object surface roughness; $d = 3.8$ for F14100 indicates a certain degree of roughness, whereas $d = 4$ for the F1850 samples denotes smooth surface. The radius of gyration R_g is associated with the object size, making sense only for diluted and monodisperse systems; the membranes under study cannot be regarded as satisfying these requisites, and therefore the reported R_g values must be taken only in a qualitative fashion.

Since the membrane performance strongly depends on the water channel structural conformation, the present work is mainly focused on the high-q region, which is therefore studied in detail. The main feature in this region is the "ionomer peak", which corresponds to the first maximum in the structure factor [47], revealing a local ordering within the ionic clusters [48]. The pattern feature called "matrix knee" is a broad shoulder peak centered around 0.07 Å^{-1}; it is usually attributed to a supralamellar distance in the crystalline part on the polymer, its magnitude depending on the degree of crystallinity [49]. In this region, SANS patterns were fitted using the addition of BPM accounting for the ionomer peak centered at q_{01} and CLM for the matrix knee region. Fig. 5 displays the high-q fitted profile and Table 2 details the values for the parameters obtained. Subindices 1 and 2 refer to BPM and CLM, respectively.

The main difference between the patterns in this region is the position and the intensity of the ionomer peak, comparing treated and untreated samples. Table 3 displays the peak FWHM (full width at half maximum) and centroid values resulting from the BPM fittings. As can be observed, in both membranes the peaks shift to lower q after treatment, the corresponding centroids decreasing ~ 20%. Consequently, in real space this corresponds to an approximate 20% increase in the characteristic structure distance d_{01}. As explained below (XRD results),

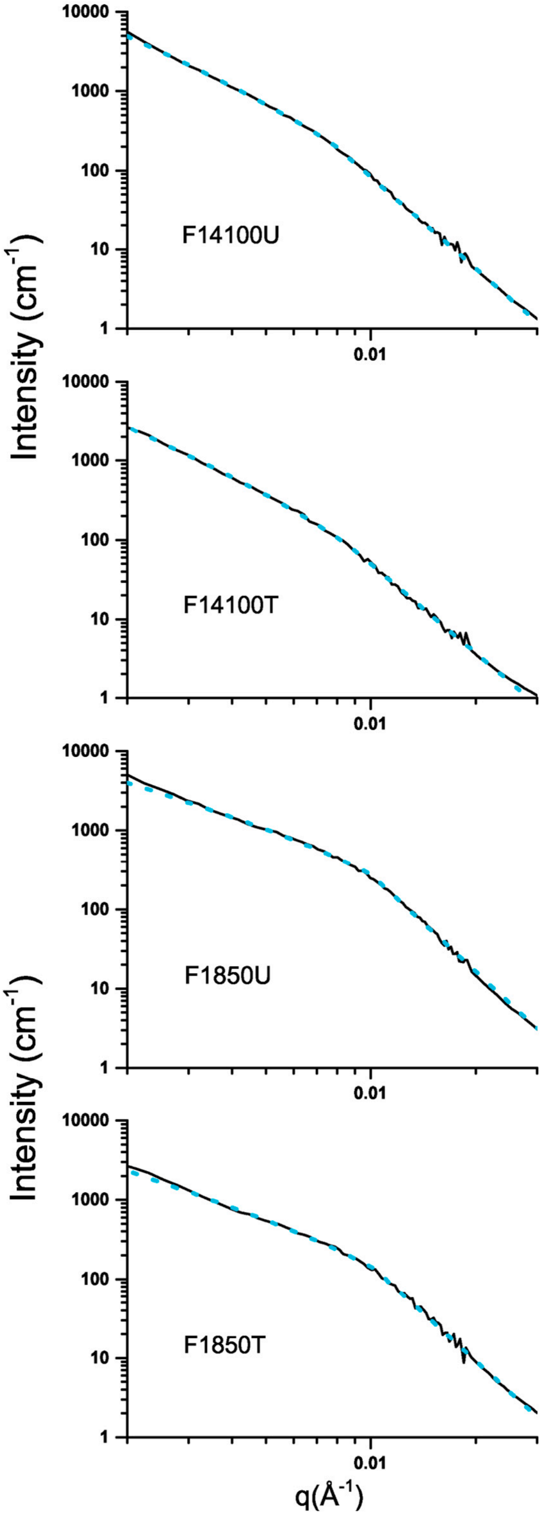

Fig. 4. Low-q empirical model fitting for the untreated (U) and treated (T) membranes. Black: experimental; cyan, dotted: GPM fitting. (For interpretation of the references to color in this figure legend, the reader is referred to the web version of this article.)

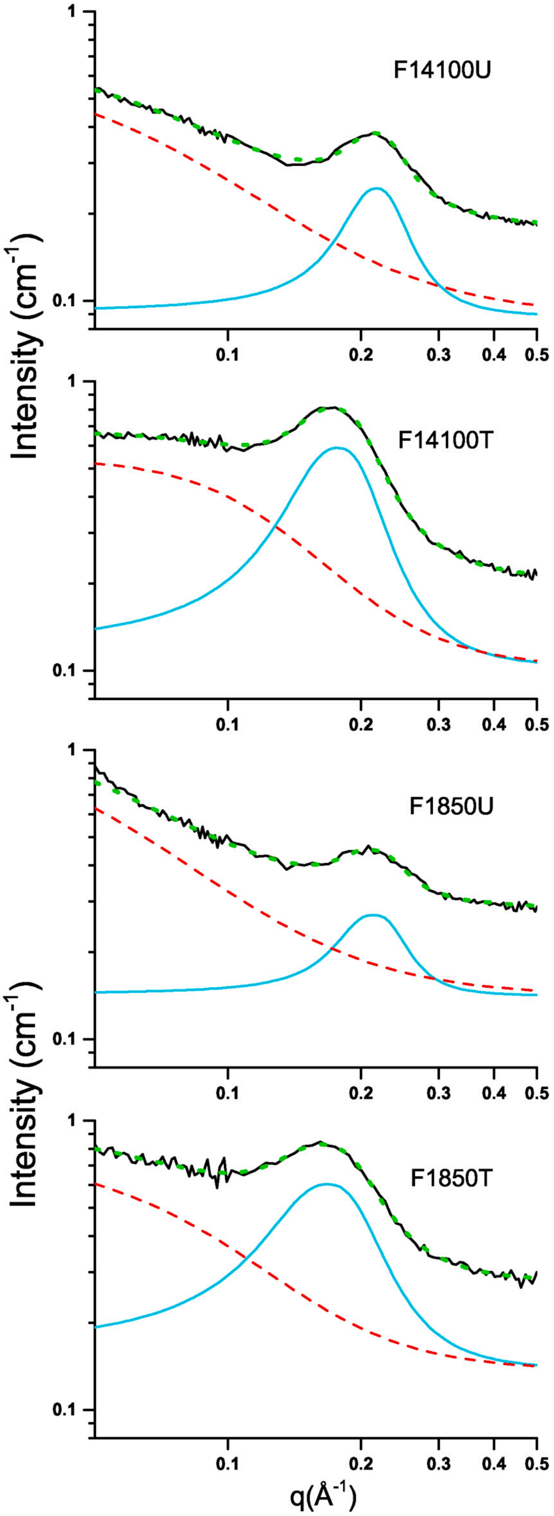

Fig. 5. Fittings of the high-q empirical models for the untreated (U) and treated (T) membranes. Black: experimental; cyan: water channel (BPM); red, dashed: crystals (CLM) and green, dotted: water channels + crystals. (For interpretation of the references to color in this figure legend, the reader is referred to the web version of this article.)

this implies a higher water absorption capacity in the treated samples, since it converts hydrophobic phases to hydrophilic domains.

The preceding results suggest a lamellar water channel structure, with correlation length d_{01}. In order to provide a detailed description, the Inverse Fourier Transform method approach has been implemented to match the SANS patterns acquired. To this purpose, scattering length density maps were furnished through the Monte Carlo simulations described above. With the aim of adequately describing the structure responsible for the ionomer peak, lamellar-structure channel clusters were built up as detailed above. In the present case, this characteristic length d_{01} is determined by the length $d_w + d_p$ spanning a water channel width (d_w) and an adjacent polymer layer (d_p). The d_{01} distance was fixed from Table 3, whereas d_w and d_p were varied, allowing fluctuations Δ_p around the latter (polymer width wall variation). It must be pointed out that although the polymer matrix is indeed teflon, the sulfonic branches are responsible for the water absorption within the conduction channels: these functional groups provide the final membrane hydrophilicity. This is the reason why the parameter d_p is varied and influences the membrane response. Similarly, the number of channels n_c contained in each cluster, as well as the average cluster lateral dimension ℓ_c were also allowed to vary along the simulation process. All these parameters were refined in order to adjust position, width and intensity of the ionomer peak. The corresponding values obtained are shown in Table 4, whereas Fig. 6 displays an example for the final scattering density map corresponding to the F14100T sample.

Table 3
Peak features from BPM results: ionomer peak position q_{01}, associated correlation length $d_{01} = 2\pi/q_{01}$ and full width at half maximum.

Sample	q_{01} (Å^{-1})	d_{01} (Å)	FWHM (Å^{-1})
F14100U	0.217 ± 0.001	29.0 ± 0.1	0.075 ± 0.001
F14100T	0.177 ± 0.001	35.5 ± 0.2	0.082 ± 0.001
F1850U	0.213 ± 0.002	29.5 ± 0.3	0.078 ± 0.001
F1850T	0.168 ± 0.002	37.4 ± 0.4	0.091 ± 0.001

Table 4
Water-channel parameters obtained by the simulation process.

Sample	d_p (Å)	d_w (Å)	Δ_p (Å)	n_c	ℓ_c (Å)
F14100U	18 ± 0.5	11 ± 1	6 ± 0.5	3–5	140 ± 5
F14100T	17 ± 0.5	18 ± 1	8 ± 0.5	3–5	150 ± 5
F1850U	18 ± 0.5	11 ± 1	7 ± 0.5	3–5	100 ± 5
F1850T	18 ± 0.5	19 ± 1	9 ± 0.5	3–5	100 ± 5

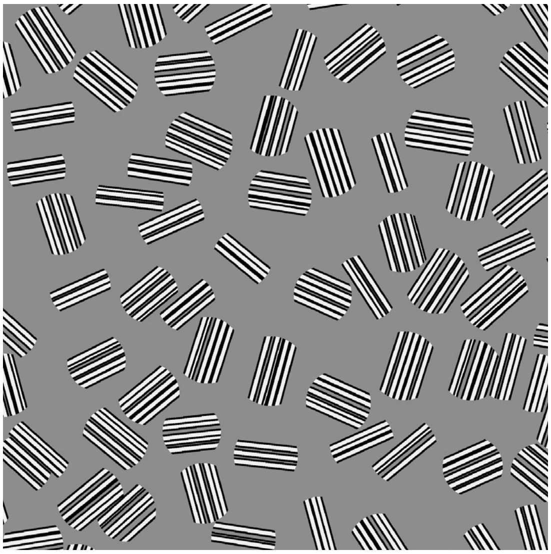

Fig. 6. Two dimensional cross section for the scattering length density map resulting from the simulations for the F14100T sample.

The other important component of the membrane structure is the crystallite content, which produces a major contribution to the scattering intensity at the matrix knee [49,50]. Since these crystallites are small 3D objects, their scattering intensity cannot be accounted

Table 5
Disc-shape parameters obtained by SASfit for the crystallite contribution to the scattering intensity.

Sample	R (Å)	L (Å)
F14100U	24 ± 1	7 ± 1
F14100T	14 ± 1	7 ± 1
F1850U	24 ± 1	7 ± 1
F1850T	15 ± 1	7 ± 1

Table 6
Peak area comparison.

Sample	Method	A_U	A_T	A_U/A_T
F14100	BPM	0.0160 ± 0.0003	0.0530 ± 0.002	0.30 ± 0.02
	Simulations	0.0142 ± 0.0003	0.0346 ± 0.001	0.41 ± 0.02
F1850	BPM	0.0131 ± 0.0003	0.0564 ± 0.002	0.23 ± 0.01
	Simulations	0.0073 ± 0.0002	0.0271 ± 0.001	0.26 ± 0.02

for through the 2D SLD maps used for the lamellar structure. For this reason, their contribution has been modeled by means of the SASfit software. The input pattern used to perform this fitting process was taken from the function obtained through CLM. The best fit was achieved by using disc shape form factors, the fitted radii R and lengths L obtained being shown in Table 5.

By adding both contributions for the membrane main structural components, the total scattering intensity is obtained and then compared with the experimental SANS pattern. Fig. 7 shows the final fits for the high-q region for all samples.

As mentioned above, the main change observed in the patterns corresponding to samples before and after treatment arises on the ionomer peak position and intensity. The activation process efficiency can be related to the ratio A_U/A_T between the peak areas A_U and A_T, respectively corresponding to the untreated and treated membranes. Table 6 displays the different ratios obtained for A_U/A_T in the samples analyzed. The differences observed can be attributed to the fact that the acid treatment applied to the membrane induces swelling of the ionic domains, as repeatedly reported in other works based on PFSA membranes [51–54]; a better connection between the hydrophilic domains is therefore achieved, *i.e.*, a higher water absorption capacity is obtained, since the spatial regions corresponding to the degraded hydrophobic phases turn into membrane hydrophilic domains [52]. These larger dimensions of the water scattering objects increase the scattered intensity. In other words, the treatment induces a random interconnection between adjacent channels, resulting in wider water channels that are irregularly spaced within the membrane structure, which correspondingly translates into the observed peak broadening.

With the aim of completing the crystalline contribution description, conventional X-ray diffraction experiments were performed. As shown in Fig. 8, the corresponding profile features are slightly different from those appearing in other perfluorosulfonic acid membranes, such as Nafion, as pointed out in ref. [55]. A main feature around 1.25 Å^{-1} can be observed, which results from the overlap of four peaks (see below), and a wide peak at $q = 2.75$ Å^{-1}, corresponding to a Bragg distance of 2.28 Å related with an intra-chain distance of the membrane [56].

The XRD patterns were fitted to deconvolve the peak contribution in the q-range between 0.7 and 1.7 Å^{-1}. Fig. 9 shows the results of these fittings, where the peak due to the amorphous polymer centered at $q \approx 1.18$ Å^{-1} overlaps with two crystalline peaks at $q \approx 1.27$ Å^{-1} and $q \approx 1.43$ Å^{-1} for all these membranes. Another small wide peak appears at $q \approx 1.48$ Å^{-1} and is associated to an amorphous component compatible with S–S first correlation shell around 4.18 Å, as reported in [57].

This fitting procedure allowed to estimate the crystallite sizes τ by using the full width at half maximum Δq in the Scherrer equation

$$\tau = \frac{5.56}{\Delta q} . \qquad (3)$$

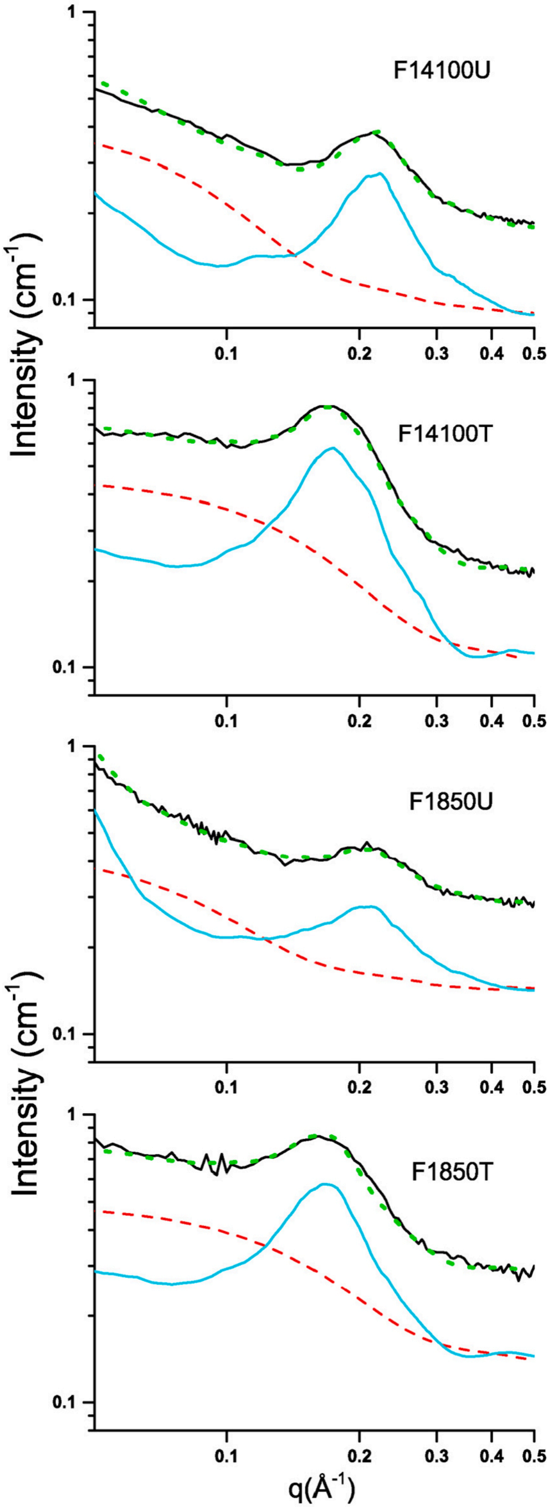

Fig. 7. Modeling of SANS patterns and comparison with experimental data in the high-q range. Black: experimental; cyan: water channels (simulations); red, dashed: crystals (SASfit) and green, dotted: water channels + crystals. (For interpretation of the references to color in this figure legend, the reader is referred to the web version of this article.)

These fits also allowed to provide a measure for the crystallinity χ_c, which was thus obtained by integrating the crystalline intensity $I_c(q)$

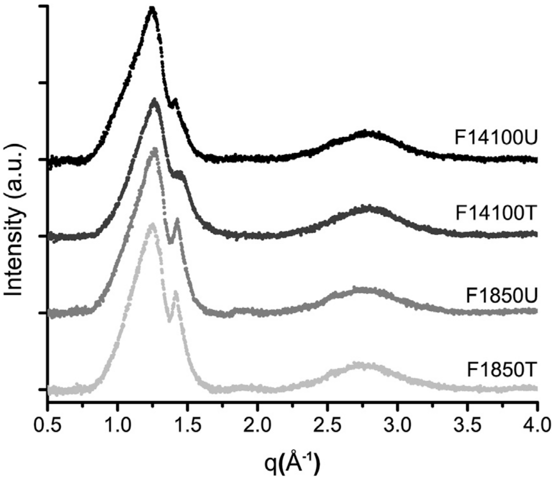

Fig. 8. X-ray diffraction patterns taken from the F14100 and F1850 membranes, before (U) and after (T) the activation treatment.

and the total intensity $I_T(q)$ according to [56]

$$\chi_c = \frac{\int q^2 I_c(q) dq}{\int q^2 I_T(q) dq}\,. \tag{4}$$

The values obtained for the crystallinity and the crystal sizes are shown in Table 7. As can be seen, the crystallinity values of around 0.25 are slightly greater than that of 0.18 obtained in a previous work for the Nafion membrane [42]; as stated in [52], an increase in this crystallinity measure could limit the transport of species, which has also been pointed out in [11]. Since these higher χ_c in treated membranes may impact on their protonic conductivity, this issue should be checked in future studies with other techniques [52]. The crystal sizes assessed with this procedure depend on the crystalline peak considered, resulting in an average value of $\tau \approx 4$ nm; these values are roughly similar to the $2R$ sizes obtained for these disc-shaped elements through the SANS pattern fittings, as displayed in Table 5.

Table 7
High q fitting parameters related to crystallinity.

Sample	χ_c	crystal size (nm)
F14100T	0.28 ± 0.02	3.8 ± 0.8
F14100U	0.27 ± 0.02	4.1 ± 0.6
F1850T	0.24 ± 0.01	3.9 ± 0.8
F1850U	0.21 ± 0.01	4.1 ± 0.4

5. Conclusions

The Fumapem F-14100 and F-1850 membrane structure and the changes produced by the activation treatment on them were characterized for the first time through SANS measurements, empirical models and Monte Carlo simulations of scattering length density maps. By fitting the empirical models to the experimental data, some structural features were obtained, such as the lamellar shape of the channels and the inter-channel distance, which were used to build up SLD maps and produce simulated SANS patterns.

The structural parameters involved in SLD maps were optimized for each sample. The comparison with the experimental data shows that the lamellar cluster model properly describes the membrane structures. In addition, it was found that the main difference between both membranes with and without the activation procedure is in the inter-channel distance due to the polymer microdegradations produced by the acid present in the treatment, resulting in the formation of new hydrophilic domains within the membrane, from surrounding membrane regions where the polymer was originally amorphous.

The proton exchange membranes studied offer an effective alternative in several fuel-cell applications, since their low cost is accompanied with an interesting performance. The nanometric structural characterization carried out will enable a new insight about their potential use in energy applications within responsible technological developments under environmental enhancement, which soon will be available for portable devices, everyday gadgets, automobile comfort, etc.

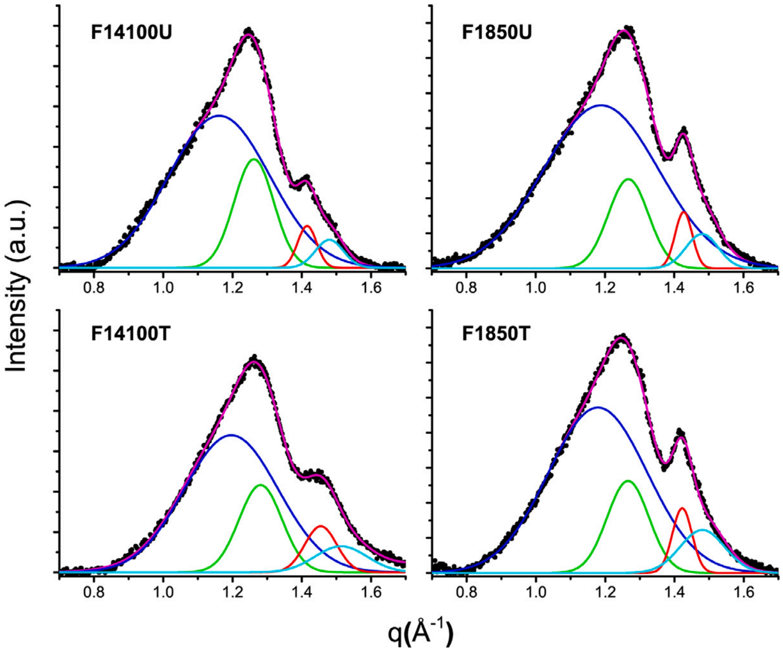

Fig. 9. XRD fittings for the patterns corresponding to the studied Fumatech samples with and without activation treatment (respectively U and T). Blue and cyan: amorphous peaks, red and green: crystalline peaks; violet: cumulative. (For interpretation of the references to color in this figure legend, the reader is referred to the web version of this article.)

Declaration of competing interest

The authors declare that they have no known competing financial interests or personal relationships that could have appeared to influence the work reported in this paper.

Acknowledgments

The authors acknowledge financial support from ANPCyT-FONCyT (Argentina), through project PICT-2016 no. 0285. They are grateful to the Institute Laue–Langevin (ILL) Grenoble, France, where the SANS measurements were taken.

References

[1] B. Dudley, BP Statistical Review of World Energy: An Unsustainable Path, BP, London, UK, 2019.

[2] A. Baroutaji, J. Carton, M. Sajjia, A. Olabi, Materials in PEM fuel cells, in: Reference Module in Materials Science and Materials Engineering, Elsevier, Netherlands, 2016.

[3] T. Wilberforce, A. Alaswad, A. Palumbo, M. Dassisti, A.-G. Olabi, Advances in stationary and portable fuel cell applications, Int. J. Hydrogen Energy 41 (37) (2016) 16509–16522.

[4] V. Neburchilov, J. Martin, H. Wang, J. Zhang, A review of polymer electrolyte membranes for direct methanol fuel cells, J. Power Sources 169 (2) (2007) 221–238.

[5] B. Ong, S.K. Kamarudin, S. Basri, Direct liquid fuel cells: A review, Int. J. Hydrogen Energy 42 (15) (2017) 10142–10157.

[6] S.P. Nunes, K.-V. Peinemann, Membrane Technology, Wiley Online Library, 2001.

[7] G. Inzelt, M. Pineri, J. Schultze, M. Vorotyntsev, Electron and proton conducting polymers: recent developments and prospects, Electrochim. Acta 45 (15–16) (2000) 2403–2421.

[8] J. Kerres, W. Cui, R. Disson, W. Neubrand, Development and characterization of crosslinked ionomer membranes based upon sulfinated and sulfonated PSU crosslinked PSU blend membranes by disproportionation of sulfinic acid groups, J. Membr. Sci. 139 (2) (1998) 211–225.

[9] W. Liu, K. Ruth, G. Rusch, et al., The membrane durability in PEM fuel cells, J. New Mater. Electrochem. Syst. 4 (4) (2001) 227–232.

[10] J. Li, M. Pan, H. Tang, Understanding short-side-chain perfluorinated sulfonic acid and its application for high temperature polymer electrolyte membrane fuel cells, RSC Adv. 4 (2014) 3944–3965.

[11] D.W. Shin, M.D. Guiver, Y.M. Lee, Hydrocarbon-based polymer electrolyte membranes: Importance of morphology on ion transport and membrane stability, Chem. Rev. 117 (6) (2017) 4759–4805.

[12] E.G. Sorte, B.A. Paren, C.G. Rodriguez, C. Fujimoto, C. Poirier, L.J. Abbott, N.A. Lynd, K.I. Winey, A.L. Frischknecht, T.M. Alam, Impact of hydration and sulfonation on the morphology and ionic conductivity of sulfonated poly(phenylene) proton exchange membranes, Macromolecules 52 (3) (2019) 857–876.

[13] K. Schmidt-Rohr, Q. Chen, Parallel cylindrical water nanochannels in nafion fuel-cell membranes, Nature Mater. 7 (2008) 75–83.

[14] K. Kreuer, G. Portale, A critical revision of the nano-morphology of proton conducting ionomers and polyelectrolytes for fuel cell applications, Adv. Funct. Mater. 23 (43) (2013) 5390–5397.

[15] M. Ahmed, I. Dincer, A review on methanol crossover in direct methanol fuel cells: challenges and achievements, Int. J. Energy Res. 35 (14) (2011) 1213–1228.

[16] N.W. Deluca, Y.A. Elabd, Polymer electrolyte membranes for the direct methanol fuel cell: a review, J. Polym. Sci. B: Polym. Phys. 44 (16) (2006) 2201–2225.

[17] X. Sun, S.C. Simonsen, T. Norby, A. Chatzitakis, Composite membranes for high temperature PEM fuel cells and electrolysers: A critical review, Membranes 9 (7) (2019).

[18] K. Miyatake, Y. Chikashige, M. Watanabe, Novel sulfonated poly (arylene ether): a proton conductive polymer electrolyte designed for fuel cells, Macromolecules 36 (26) (2003) 9691–9693.

[19] F. Lufrano, V. Baglio, P. Staiti, V. Antonucci, et al., Polymer electrolytes based on sulfonated polysulfone for direct methanol fuel cells, J. Power Sources 179 (1) (2008) 34–41.

[20] M. Gil, X. Ji, X. Li, H. Na, J.E. Hampsey, Y. Lu, Direct synthesis of sulfonated aromatic poly (ether ether ketone) proton exchange membranes for fuel cell applications, J. Membr. Sci. 234 (1–2) (2004) 75–81.

[21] Y. Woo, S.Y. Oh, Y.S. Kang, B. Jung, Synthesis and characterization of sulfonated polyimide membranes for direct methanol fuel cell, J. Membr. Sci. 220 (1–2) (2003) 31–45.

[22] J. Kerres, V. Atanasov, Cross-linked PBI-based high-temperature membranes: Stability, conductivity and fuel cell performance, Int. J. Hydrogen Energy 40 (42) (2015) 14723–14735.

[23] D. Villa, S. Angioni, E. Quartarone, P. Righetti, P. Mustarelli, New sulfonated PBIs for PEMFC application, Fuel Cells 13 (1) (2013) 98–103.

[24] S. Angioni, D.C. Villa, S. Dal Barco, E. Quartarone, P.P. Righetti, C. Tomasi, P. Mustarelli, Polysulfonation of PBI-based membranes for HT-PEMFCs: a possible way to maintain high proton transport at a low H_3PO_4 doping level, J. Mater. Chem. A 2 (3) (2014) 663–671.

[25] A. Aricò, D. Sebastian, M. Schuster, B. Bauer, C. D'Urso, F. Lufrano, V. Baglio, Selectivity of direct methanol fuel cell membranes, Membranes 5 (4) (2015) 793–809.

[26] V. Baglio, A. Stassi, O. Barbera, G. Giacoppo, D. Sebastian, C. D'Urso, M. Schuster, B. Bauer, J. Bonde, A. Aricò, Direct methanol fuel cell stack for auxiliary power units applications based on FUMAPEM® F-1850 membrane, Int. J. Hydrogen Energy 42 (43) (2017) 26889–26896.

[27] I.M. Krivobokov, E.N. Gribov, A.G. Okunev, Proton conducting hydrocarbon membranes: Performance evaluation for room temperature direct methanol fuel cells, Electrochim. Acta 56 (5) (2011) 2420–2427.

[28] H.F. Mohamed, E. Abdel-Hady, M. Abdel-Hamed, Proton conductivity and free volume properties in per-fluorinated sulfonic acid/PTFE copolymer for fuel cell, Acta Phys. Polon. A. 132 (5) (2017).

[29] M.-H. Kim, C.J. Glinka, S.A. Grot, W.G. Grot, SANS study of the effects of water vapor sorption on the nanoscale structure of perfluorinated sulfonic acid (nafion) membranes, Macromolecules 39 (14) (2006) 4775–4787.

[30] S. Deabate, G. Gebel, P. Huguet, A. Morin, G. Pourcelly, 3 in situ and operando determination of the water content distribution in proton conducting membranes for fuel cells: a critical review, Energy Environ. Sci. 5 (2012) 8824–8847.

[31] C.J. Jafta, X.-G. Sun, G.M. Veith, G.V. Jensen, S.M. Mahurin, M.P. Paranthaman, S. Dai, C.A. Bridges, Probing microstructure and electrolyte concentration dependent cell chemistry via operando small angle neutron scattering, Energy Environ. Sci. 12 (2019) 1866–1877.

[32] R. Kuwertz, C. Kirstein, T. Turek, U. Kunz, Influence of acid pretreatment on ionic conductivity of Nafion® membranes, J. Membr. Sci. 500 (2016) 225–235.

[33] E.Y. Safronova, A.K. Osipov, A.B. Yaroslavtsev, Short side chain Aquivion perfluorinated sulfonated proton-conductive membranes: transport and mechanical properties, Pet. Chem. 58 (2) (2018) 130–136.

[34] B. Hammouda, A new Guinier–Porod model, J. Appl. Crystallogr. 43 (4) (2010) 716–719.

[35] O. Glatter, O. Kratky, Small Angle X-Ray Scattering, Academic press, 1982.

[36] R.P. Hjelm Jr., P. Thiyagarajan, H. Alkan-Onyuksel, Organization of phosphatidylcholine and bile salt in rodlike mixed micelles, J. Phys. Chem. 96 (21) (1992) 8653–8661.

[37] G. Yuan, X. Wang, D. Wu, B. Hammouda, Structural analysis of dendrimers based on polyhedral oligomeric silsesquioxane and their assemblies in solution by small-angle neutron scattering: Fits to a modified two correlation lengths model, Polymer 100 (2016) 119–125.

[38] B. Hammouda, Probing Nanoscale Structures-The Sans Toolbox, National Institute of Standards and Technology, 2008, pp. 1–717.

[39] T. Kureha, T. Sato, D. Suzuki, Relationship between temperature-induced changes in internal microscopic structures of poly(N-isopropylacrylamide) microgels and organic dye uptake behavior, Langmuir 30 (29) (2014) 8717–8725.

[40] R. Hiesgen, T. Morawietz, M. Handl, M. Corasaniti, K.A. Friedrich, Insight into the structure and nanoscale conductivity of fluorinated ionomer membranes, J. Electrochem. Soc. 161 (12) (2014) F1214–F1223.

[41] J.S. da Silva, S.G.M. Carvalho, R.P. da Silva, A.C. Tavares, U. Schade, L. Puskar, F.C. Fonseca, B.R. Matos, SAXS signature of the lamellar ordering of ionic domains of perfluorinated sulfonic-acid ionomers by electric and magnetic field-assisted casting, Phys. Chem. Chem. Phys. 22 (2020) 13764–13779.

[42] S. Fernandez Bordín, H. Andrada, A. Carreras, G. Castellano, R. Oliveira, V. Galván Josa, Nafion membrane channel structure studied by small-angle X-ray scattering and Monte Carlo simulations, Polymer 155 (2018) 58–63.

[43] K. Schmidt-Rohr, Simulation of small-angle scattering curves by numerical fourier transformation, J. Appl. Crystallogr. 40 (1) (2007) 16–25.

[44] S.C. DeCaluwe, P.A. Kienzle, P. Bhargava, A.M. Baker, J.A. Dura, Phase segregation of sulfonate groups in Nafion interface lamellae, quantified via neutron reflectometry fitting techniques for multi-layered structures, Soft Matter 10 (2014) 5763–5776.

[45] I. Breßler, J. Kohlbrecher, A.F. Thünemann, *SaSfit*: a tool for small-angle scattering data analysis using a library of analytical expressions, J. Appl. Crystallogr. 48 (5) (2015) 1587–1598.

[46] V. Galván Josa, H.E. Andrada, G.E. Castellano, E. Castellano-Hernández, G.J. Cuello, S.P. Fernandez Bordín, S.P. Limandri, C. Mondelli, R. Schweins, Structural Characterization of Proton Exchange Membrane Fuel Cells, Institut Laue-Langevin (ILL), 2018, http://dx.doi.org/10.5291/ILL-DATA.1-04-132.

[47] L. Rubatat, A.L. Rollet, G. Gebel, O. Diat, Evidence of elongated polymeric aggregates in nafion, Macromolecules 35 (10) (2002) 4050–4055.

[48] G. Gebel, O. Diat, Neutron and X-ray scattering: Suitable tools for studying ionomer membranes, Fuel Cells 5 (2) (2005) 261–276.

[49] T.D. Gierke, G.E. Munn, F.C. Wilson, The morphology in nafion perfluorinated membrane products, as determined by wide- and small-angle x-ray studies, J. Polym. Sci.: Polym. Phys. Ed. 19 (11) (1981) 1687–1704.

[50] C.K. Knox, G.A. Voth, Probing selected morphological models of hydrated nafion using large-scale molecular dynamics simulations, J. Phys. Chem. B 114 (9) (2010) 3205–3218.

[51] M. Zatoń, J. Rozière, D.J. Jones, Current understanding of chemical degradation mechanisms of perfluorosulfonic acid membranes and their mitigation strategies: a review, Sustain. Energy Fuels 1 (2017) 409–438, http://dx.doi.org/10.1039/C7SE00038C.

[52] A. Kusoglu, A.Z. Weber, New insights into perfluorinated sulfonic-acid ionomers, Chem. Rev. 117 (3) (2017) 987–1104.

[53] T. Tsuneda, R.K. Singh, A. Iiyama, K. Miyatake, Theoretical investigation of the H_2O_2-induced degradation mechanism of hydrated Nafion membrane via ether-linkage dissociation, ACS Omega 2 (7) (2017) 4053–4064.

[54] F.D. Coms, T.J. Fuller, C.P. Schaffer, A mechanistic study of perfluorosulfonic acid membrane water permeance degradation in air, J. Electrochem. Soc. 165 (6) (2018) F3104–F3110.

[55] J. Vrána, J. Charvát, P. Mazúr, P. Bělský, J. Dundálek, J. Pocedič, J. Kosek, Commercial perfluorosulfonic acid membranes for vanadium redox flow battery: Effect of ion-exchange capacity and membrane internal structure, J. Membr. Sci. 552 (2018) 202–212.

[56] P.C. van der Heijden, L. Rubatat, O. Diat, Orientation of drawn Nafion at molecular and mesoscopic scales, Macromolecules 37 (14) (2004) 5327–5336.

[57] I.H. Hristov, S.J. Paddison, R. Paul, Molecular modeling of proton transport in the short-side-chain perfluorosulfonic acid ionomer, J. Phys. Chem. B 112 (10) (2008) 2937–2949.